Front. Earth Sci. 2017, 11(2): 332–346
DOI 10.1007/s11707-016-0588-x

RESEARCH ARTICLE

Tide- and wind-driven variability of water level in Sansha Bay, Fujian, China

Hongyang LIN[1,2], Jianyu HU[1], Jia ZHU (✉)[1], Peng CHENG[1], Zhaozhang CHEN[1], Zhenyu SUN[1], Dewen CHEN[3]

1 State Key Laboratory of Marine Environmental Science, College of Ocean and Earth Sciences, Xiamen University, Xiamen 361102, China
2 College of the Environment and Ecology, Xiamen University, Xiamen 361102, China
3 Marine Forecast Station of Xiamen, State Oceanic Administration, Xiamen 361012, China

Abstract This study analyzes water-level variability in Sansha Bay and its adjacent waters near Fujian, China, using water-level data observed from seven stations along the coast and wind data observed from a moored buoy near Mazu Island. At super- to near-inertial frequencies, tides dominated the water-level variations, mainly characterized by semi-diurnal (primarily M_2, S_2, and N2) and diurnal tides (primarily K_1, O_1). The correlation coefficients between residual (non-tidal) water-level time series and the observed wind-stress time series exceeded 0.78 at all stations, hinting that the wind acting on the study region was another factor modulating the water-level variability. A cross-wavelet and wavelet-coherence analysis further indicated that (i) the residual water level at each station was more coherent and out-of-phase with the alongshore winds mostly at sub-inertial time scales associated with synoptic weather changes; and (ii) the residual water-level difference between the outer and inner bay was more coherent with the cross-shore winds at discrete narrow frequency bands, with the wind leading by a certain phase. The analysis also implied that the monsoon relaxation period was more favorable for the formation of the land-sea breeze, modulating the residual water-level difference.

Keywords residual water level, tide, wind, Sansha Bay

1 Introduction

Sansha Bay is a semi-enclosed bay located in the northeastern coastal region of Fujian Province, China. The bay has a total area of approximately 675 km^2, and is connected to the Taiwan Strait through a narrow channel approximately 3 km wide at the southeastern Bay as shown in Fig. 1. It has historically been a sheltered bay (Wang et al., 2009) and has long been known as the spawning ground of the large yellow croaker. In recent years, however, the water quality and ecosystem of the bay have deteriorated due to eutrophication. Consequently, studies on Sansha Bay have focused primarily on biological, chemical, and ecological issues (Lin et al., 1998; Cai et al., 2007). In contrast, physical oceanographic aspects of Sansha Bay have not been well understood due in part to limited observations. Our study aimed to understand the response of residual water level to wind forcing in Sansha Bay and its adjacent waters using the observed data of water level and wind. The residual water level in this study is defined as the difference between observed water level and its tidal constituents obtained via tidal harmonic analysis, i.e., the de-tided component.

Sea level response to winds in coastal regions has been investigated for decades (Csanady, 1982). Attention has been paid mostly to the role of alongshore wind in modulating sea level changes along the coast via Ekman transport, which builds up a cross-shore pressure gradient that is geostrophically balanced by alongshore currents (Smith, 1974; Ryan and Noble, 2007). In contrast, sea level variability caused by cross-shore wind is usually considered to be secondary or negligible (Csanady, 1982), unless the wind field is spatially nonuniform (Csanady, 1980). The orientation of the coastline and water depth may also play a role in modulating sea level response to wind forcing in different directions. For example, Chuang and Wiseman (1983) examined the relative importance of alongshore and cross-shore winds on sea level variability along the shelf of the northern Gulf of Mexico, and found that the different responses were caused primarily by the varying water depth.

The theory of ocean response to periodic wind forcing at a given frequency is well established (Craig, 1989a, b). A typical example of the regular wind forcing is the land-sea

Received October 28, 2015; accepted February 28, 2016

E-mail: zhujia@xmu.edu.cn

breeze, which varies diurnally with winds blowing onshore in daytime and offshore at nighttime. Ocean response (including sea level and currents) to such cross-shore winds is reported and dynamically interpreted in a variety of locations based on observations and numerical simulations (Clancy et al., 1979; Vesecky et al., 1997; Gallop et al., 2012). In particular, near the critical latitudes (approximately 30°N and 30°S), an amplified ocean response is often observed because the frequency of diurnal forcing (e.g., sea breeze) coincides with the local inertial frequency, and hence a near resonance occurs (Simpson et al., 2002; Zhang et al., 2009; Nam and Send, 2013).

In our study, we investigated the tide- and wind-driven water-level variations in Sansha Bay and its adjacent waters, noting that tides and the wind acted on different time scales. Limited by the time span of the observed data, we studied the tidal forcing at super- to near-inertial frequencies (mostly semi-diurnal and diurnal), while we studied the wind forcing at near- to sub-inertial time scales (0.5−8 d). In particular, the response of residual water level to alongshore and cross-shore winds at different frequencies was investigated. The contemporaneously collected time series of water level and winds in the study region made this air-sea coupling study possible. This paper is organized as follows. The observed data and methods used in the present study are described in Sections 2 and 3, while variations of water levels caused by tides and the wind are analyzed in Sections 4 and 5, based on tidal harmonic, spectral, and wavelet analysis. Section 6 includes a summary and discussion.

2 Data

The observed water-level time series were collected using seven water-level gauges deployed in Sansha Bay and its adjacent waters for the period 20 January to 9 March, 2013. The gauge locations are shown with black dots and with the station names labeled in Fig. 1. Each time series had a sampling interval of 10 min.

The wind data with a sampling interval of 15 min were collected from the Mazu Buoy, which is located to the south of Sansha Bay and indicated by the black triangle in Fig. 1. The wind speeds and directions were provided by the Central Weather Bureau of Taiwan (http://cwb.gov.tw/V7/observe/). Wind directions were recorded as the traditional compass rose of 16 winds, being the eight principal winds (i.e., N, NE, E, SE, S, SW, W, and NW) augmented by eight half-winds bisecting the angles between the principal winds.

3 Method

A brief description of the statistical methods used in this study is provided in this section, including tidal analysis, spectral analysis, and wavelet analysis.

3.1 Tidal analysis

We used the t_tide Matlab package (Pawlowicz et al., 2002) to perform the tidal analysis. Similar to classic harmonic analysis, t_tide predicts the tidal signal as the sum of a finite set of sinusoids at particular frequencies associated with astronomical parameters (Pawlowicz et al., 2002). The residual water level is then obtained by subtracting the tidal signal from the raw water level.

The number of tidal constituents used to model the tidal signal is determined by the time interval and span of the observed water-level time series. Given the sampling interval of every 10 min and the length of each time series of approximately 50 d, there are 35 tidal constituents used by t_tide in the harmonic analysis, with frequencies ranging from 0.0015 (the MM tidal constituent) to 0.3220 (the M_8 tidal constituent) cycles per hour.

3.2 Spectral analysis

The multi-taper method (Thomson, 1982; Percival and Walden, 1993) was applied to perform spectral analysis of the total and de-tided water-level time series. Spectral estimation is normally derived by computing the power spectral density of the time series through Fourier transform. Such a method, however, suffers from being a biased estimate of the true power spectrum. The multi-taper method, on the other hand, uses a small set of tapers to smooth the sample power spectral densities reducing the variance of the raw spectra and hence provides more confidence in spectral estimation.

Another important issue associated with spectral analysis is to assess the statistical significance of well-defined spectral peaks. Variables in geophysical or climate systems tend to have increasing power with decreasing frequency, and hence a red-noise background is usually taken as the null hypothesis (Hasselmann, 1976; Torrence and Compo, 1998). Our study also applied such a hypothesis using a first-order autoregressive [AR(1)] process to conduct the significance test. The power spectrum of an AR(1) process is estimated as (Mann and Lees, 1996):

$$P(f) = P_0 \frac{1-r^2}{1+r^2-2r\cos(\pi f/f_N)}, \quad (1)$$

where P_0 is the average value of the power spectrum, f is frequency, f_N is the Nyquist frequency, and r is the lag-one autocorrelation. Spectral peaks are considered as significant if their spectra are larger than the red-noise spectrum at the same frequency under a specified level (normally 5%, i.e., the 95% confidence level). The red-noise spectrum is determined from appropriate quantiles of the

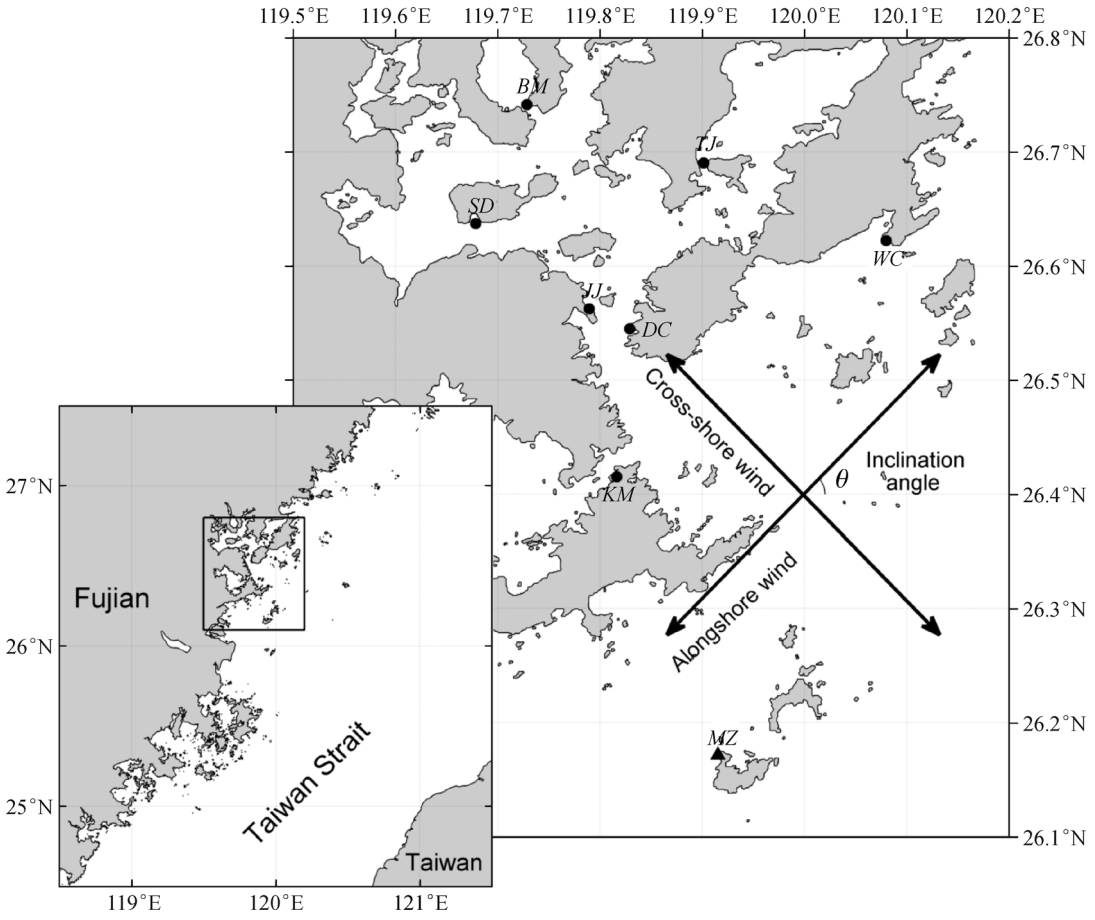

Fig. 1 Map of Sansha Bay and its adjacent waters. The dots denote water-level stations (*BM*-Baima, *TJ*-Taijiang, *SD*-Sandu, *JJ*-Jianjiang, *DC*-Dongchong, *KM*-Kemen, *WC*-Waicheng). The triangle denotes the Mazu (*MZ*) Buoy where the wind data were obtained. The arrows schematically show the alongshore and cross-shore wind directions. The wind inclination angle θ, which is the angle between the wind direction and a horizontal line, is also shown.

chi-squared distribution with $2K$ degrees of freedom and K is the number of tapers (Mann and Lees, 1996).

3.3 Wavelet analysis

Because of the inherent limitations of Fourier transform (e.g., inability to handle nonstationary processes), wavelet analysis was also used in our study to investigate variability of the wind and its interaction with water-level variations. Wavelet analysis has been widely used to study multi-scale, nonstationary processes in geophysical science since the 1980s (Morlet, 1983; Farge, 1992; Meyers et al., 1993; Lau and Weng, 1995). Wavelet analysis is superior to Fourier analysis in two aspects: (i) wavelet analysis is able to reflect time-varying characteristics of the spectra; and (ii) wavelet analysis can handle nonstationary processes, to which the variability of many atmospheric variables (e.g., wind speed) belongs.

The base functions of wavelet transform are called wavelets that can be dilated and translated in both frequency and time. Wavelet analysis is based on a set of functions $\psi_{b,a}(t)$ derived from a chosen mother wavelet $\psi(t)$:

$$\psi_{b,a}(t) = \frac{1}{a^{1/2}}\psi\left(\frac{t-b}{a}\right), \tag{2}$$

where a and b are the dilation (scale) and translation (position) parameters,; and $\psi_{b,a}(t)$ are called daughter wavelets or wavelets (Lau and Weng, 1995). The normalization factor $a^{-1/2}$ ensures that $\psi_{b,a}(t)$ has the same variance of $\psi(t)$. The convolution of a series/signal of interest, $x(t)$, with the set of wavelets is defined to be the wavelet transform (Lau and Weng, 1995):

$$W(b,a) = \frac{1}{a^{1/2}}\int \psi^*\left(\frac{t-b}{a}\right)x(t)\mathrm{d}t, \tag{3}$$

where ψ^* is the complex conjugate of ψ. In this way a one-dimensional time series is expanded into a two-dimensional (b, a) space showing the amplitude of variations at scale a and time b. This differs from Fourier transform which yields an average amplitude over time (Meyers

et al., 1993). Based on the previous theoretical framework of wavelet transform, Torrence and Compo (1998) provide a practical toolkit to apply wavelet analysis and also include statistical significance testing.

While a myriad of studies perform wavelet analysis on a single time series, previous investigators further developed the cross-wavelet transform and wavelet coherence in order to examine the link between two time series (Liu, 1994; Torrence and Webster, 1999). Suppose W_X and W_Y denote the wavelet transform of $x(t)$ and $y(t)$, then their cross-wavelet transform is defined to be (Torrence and Webster, 1999):

$$W_{XY} = W_X W_Y^*. \tag{4}$$

The amplitude of W_{XY} denotes the common power of W_X and W_Y, and its phase represents the relative phase between $x(t)$ and $y(t)$ in time and frequency space. Similar to Fourier analysis, one needs to smooth the cross spectrum before calculating coherency, and the wavelet coherence is based on smoothing in both time and scale. Following Torrence and Webster (1999), the wavelet coherence is defined to be:

$$R^2(a) = \frac{|\langle a^{-1} W_{XY}(a)\rangle|^2}{\langle a^{-1}|W_X(a)|^2\rangle \langle a^{-1}|W_Y(a)|^2\rangle}, \tag{5}$$

where a is the scale, and the chevrons denote smoothing in both time and scale. R^2 finds significant coherency between the two time series of interest even though their common power is low (Grinsted et al., 2004). Building on the work of Torrence and Webster (1999), Grinsted et al. (2004) provide an easy-to-use package for users to calculate the cross-wavelet transform and wavelet coherence, and this package was used in our study.

4 Tide-driven variability of water levels

The variation of water-level time series caused by tides was examined by applying tidal harmonic analysis and spectral analysis and is discussed in this section.

4.1 Tidal harmonic analysis

Observed water-level time series were first examined in order to gain a general insight into the temporal variability of the water levels in Sansha Bay. Figures 2(a)−2(g) show the raw water-level time series at all seven stations. Tidal modulation of the water-level variability is clearly seen in all of the time series, with a tidal range of approximately 6−7 m during spring tides and 2−3 m during neap tides. Closer inspection suggested that the raw water levels around Sansha Bay were characterized by regular semi-diurnal tides, which was verified using spectral analysis, (see below). The tidal ranges of the raw water-level time series were highest at the three most inner stations (Baima, Taijiang, Sandu), reaching approximately 7.5 m during spring tides and 3 m during neap tides. The tidal ranges then decreased with distance from the head to the mouth of the bay. For station Waicheng, the tidal range was approximately 6 m during spring tides and 2 m during neap tides. In addition, by zooming in to visualize the timing of the peaks and troughs, it could be seen that the three innermost stations had the same high- and low-water time. The above two features suggested that the tidal waves within Sansha Bay were characterized by the category of a narrow semi-enclosed bay (Walters et al., 1985). The amplitude and phase of the major tidal constituents (e.g., M_2, S_2, N_2, K_1, O_1) obtained from the tidal harmonic analysis of individual water-level time series also agreed with such features. The tidal signals first appeared at Waicheng with the smallest range, and then appeared later with amplified, and approximately the same, ranges in the inner bay. We therefore inferred that the propagating tidal waves progressed from the open sea to Sansha Bay, which then turned into standing waves caused by wave reflection within this narrow semi-enclosed bay.

The residual water-level time series are shown correspondingly in the right panels of Fig. 2. The range of residual water level was smaller than the raw water level by a factor of 6 to 7, implying that water-level variation around the bay was tide-dominant. It was interesting to note that all of the residual water-level time series shared a rather similar shape in terms of time variation, hinting that they were probably driven by a common forcing. This external forcing was believed to be the winds prevailing in Sansha Bay and its adjacent area, and are investigated in Section 5.

In addition to the analysis at individual stations, water-level difference between the outer and inner bay were also of interest in our study. Stations Waicheng, Kemen, and Dongchong were chosen as outer stations, and Baima, Sandu, and Taijiang as inner stations (Fig. 1). For simplicity, we denoted the raw (residual) water level at Waicheng and Baima as $\eta^{WC}(\eta^{WC}_{res})$ and $\eta^{BM}(\eta^{BM}_{res})$, and their difference as $\eta^{WC-BM}(\eta^{WC-BM}_{res})$. This notation was followed at other stations (the abbreviation of each station name is listed in the caption of Fig. 1). We chose Waicheng and Kemen as outer stations, and Baima and Sandu as inner stations, to examine the variability of η^{WC-BM}, η^{WC-SD}, η^{KM-BM} and η^{KM-SD}, as well as their residuals.

It can be seen from Fig. 3 that the difference of raw water levels between the outer and inner bay had similar frequencies to their individual raw water levels. The spring-neap tides could also be seen in the water-level differences. The amplitudes of water-level differences were all much smaller compared to their individual amplitudes (comparing left panels of Figs. 2 and 3). In addition, the tidal ranges of η^{WC-BM} and η^{WC-SD} were larger than those of η^{KM-BM} and η^{KM-SD} by a factor of

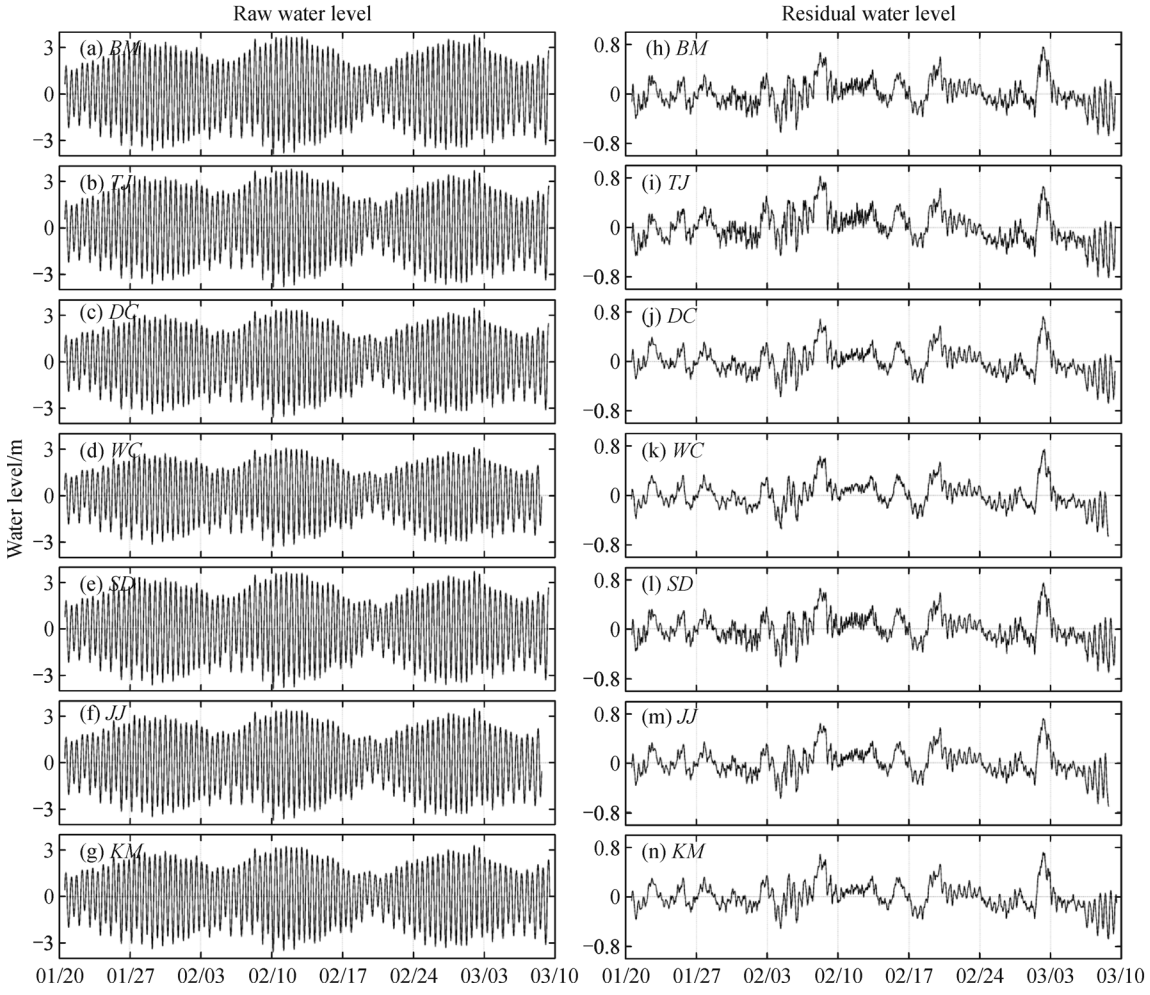

Fig. 2 Time series of the (left) raw and (right) residual water level at all stations.

about two. This was because the phase lags between tidal signals at Kemen and the inner stations were smaller than the lags between Waicheng and the inner stations: the quasi-synchrony cancelled out most peak-to-peak amplitudes resulting in smaller tidal ranges. The residual water-level differences (right panels of Fig. 3) clearly indicated more high-frequency variability compared to the raw differences. Unlike residual water level at individual stations (right panels of Fig. 2), there was no clear low-frequency modulation in the residual water-level differences. The ranges of residual water-level differences were generally less than 0.4 m, and hence smaller compared to those of individual residual water levels.

4.2 Spectral analysis

A set of power spectral analyses were performed on the raw and residual water-level time series at individual stations. In general, they shared qualitatively similar spectral shapes at all seven stations (Fig. 4). The spectra of the raw water levels all had the highest energy peak at a frequency of approximately 2 cycles per day (cpd) and the second highest peak at approximately 1 cpd. In other words, the raw water-level time series in Sansha Bay were characterized primarily by semi-diurnal tides, followed by diurnal tides. Furthermore, a significant spectral peak at a frequency of approximately 4 cpd could also be identified at the three most inner stations (Figs. 4(a), 4(b), and 4(e)), and the tidal harmonic analysis suggested that it was contributed mainly by tidal constituents M_4 and MS_4. The power spectra of the residual water-level time series are shown in the right panels of Fig. 4. The spectral peaks of the residual water levels were not as pronounced as those of the raw water levels. Overall, variations at frequencies close to the diurnal and semi-diurnal periods could still be discerned in the power spectra of residual water levels, although the amplitudes were much smaller and the peaks "flatter" compared to the spectra of their raw water levels. Moreover, the residual water levels also included lower-frequency variability with a period of 2−3 d, which was not seen in the raw water-level spectra. The high-frequency spectral peaks also became more apparent in the residual

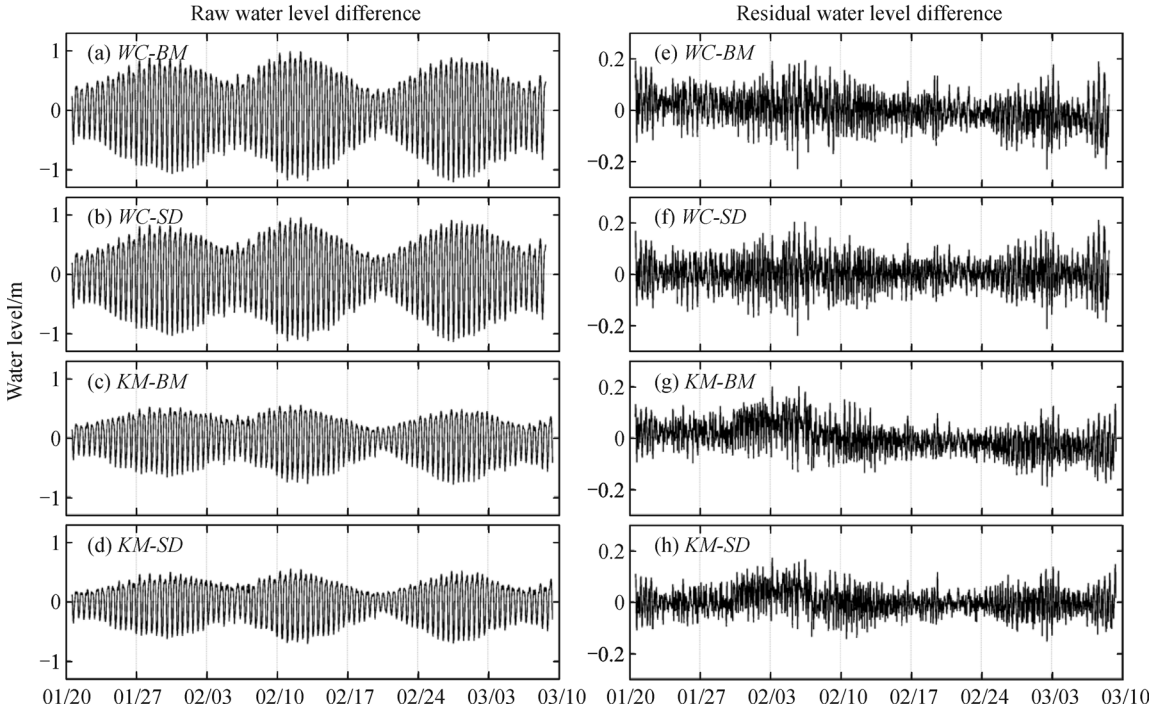

Fig. 3 Differences of the (left) raw and (right) residual water level between outer and inner stations. The upper two rows of panels relate to differences between Waicheng with Baima and Sandu; and the lower two rows between Kemen with Baima and Sandu.

water-level spectra.

The power spectra of the water-level differences between the outer and inner bay showed well-defined spectral peaks all at super-inertial time scales. The raw water-level differences had relatively sharp and significant spectral peaks at frequencies of approximately 2, 4, and 6 cpd (left panels of Fig. 5). There was also a peak at 8 cpd if Kemen was chosen as the outer station. The residual water-level differences (right panels of Fig. 5) showed spectral peaks at similar frequencies as the raw water-level differences (left panels of Fig. 5), although the amplitudes were smaller and the semi-diurnal peak no longer predominant. In addition, more high-frequency spectral peaks were more noticeable in the spectra of residual water-level differences, consistent with the results shown in Fig. 3.

5 Wind-driven variability of water levels

The previous section describes water-level changes in Sansha Bay contributed by tides. In this section the variability of water levels caused by winds prevailing in the study region is discussed, mostly based on wavelet analysis.

5.1 Variability of wind forcing

As mentioned above, wind forcing, in addition to tides, may be a factor in modulating water-level variations in Sansha Bay. We thus examined first the time series of wind vectors and its spectral features. The time-varying wind vectors observed at the Mazu Buoy are shown in Fig. 6, which shows that the north-northeasterly (NNE) wind was prevailing in the winter monsoon season followed by northerly and northeasterly winds, implying that the study region was dominated by down-welling favorable winds during the observation period. It is also clear from Fig. 6 that the prevailing NNE wind was stronger and more persistent between 5 and 25 February 2013 with a magnitude exceeding 10 $m \cdot s^{-1}$. In the other periods, the wind was weaker and even occasionally reversed.

Since the atmospheric variables in the Northern Hemisphere are most dynamically active in winter, in order to resolve nonstationary processes we used wavelet power analysis instead of Fourier power analysis to examine the spectral features of the winds in the study region. The wavelet power spectrum of the wind speed (Fig. 7) showed two relatively prominent periods of approximately 2−3 d and 0.5−1 d. The former period was probably due to synoptic weather changes, while the latter was potentially associated with changes in the land-sea breeze.

5.2 Correlation between water levels and the wind

The spectral analyses of residual water levels and the wind both indicated a period of approximately 2−3 d as well as quasi-diurnal variability. The common spectral peaks hint

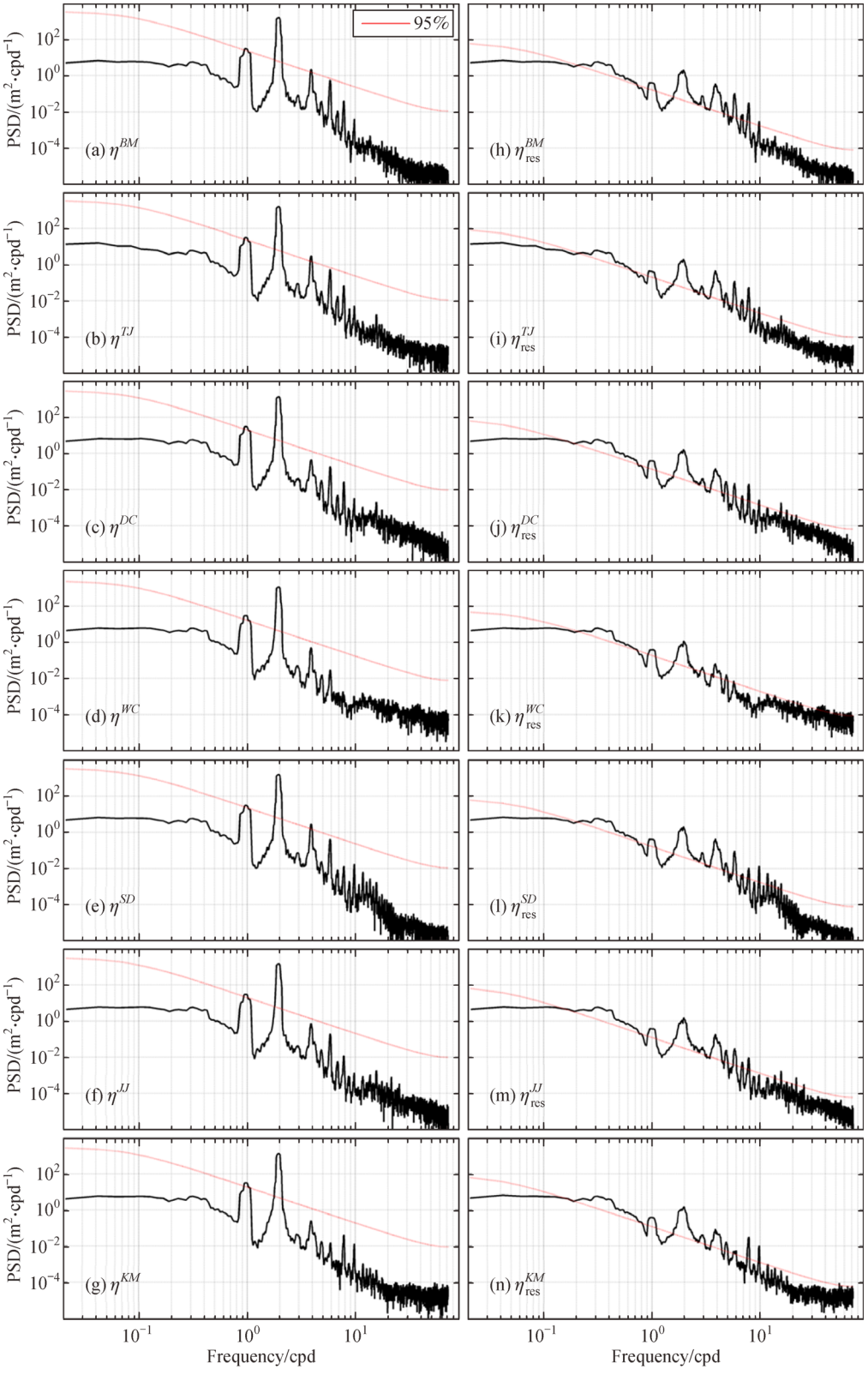

Fig. 4 Power spectral densities of the (left) raw and (right) residual water levels at individual stations. The red dashed line in each panel denotes the 95% confidence level assuming a red-noise null hypothesis.

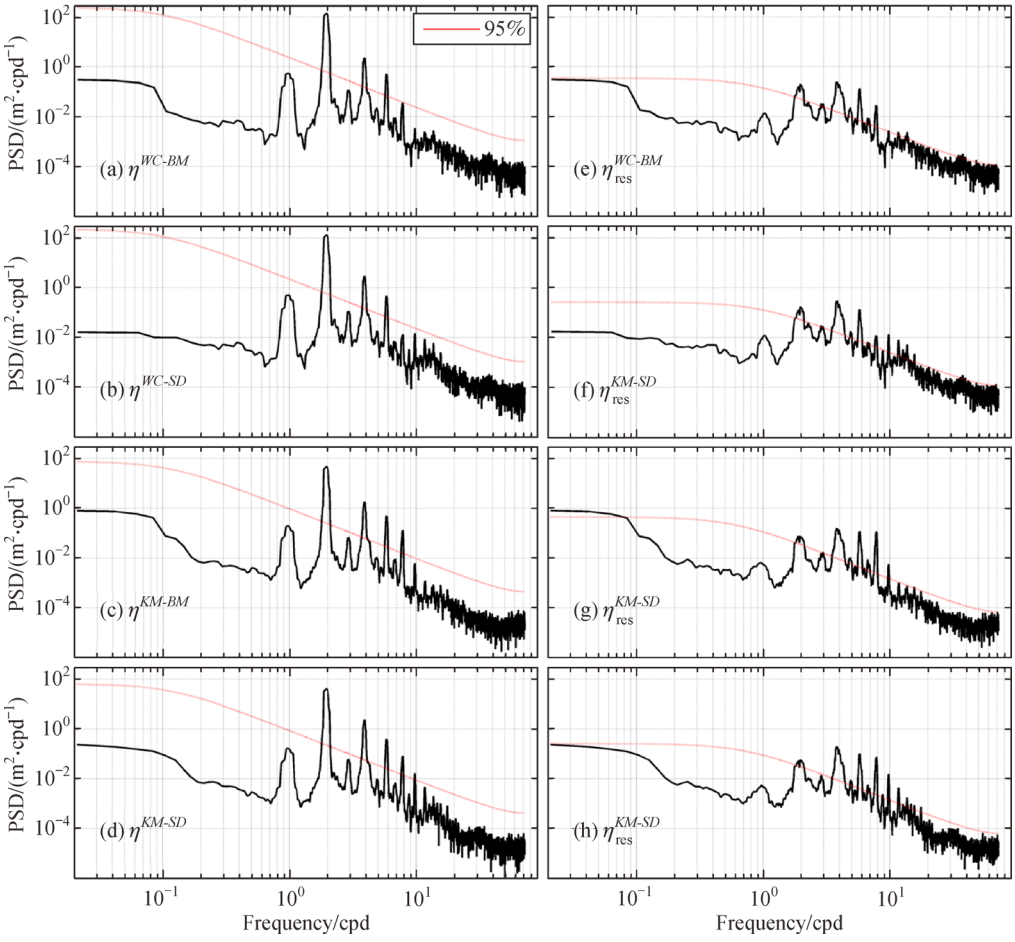

Fig. 5 Similar format as Fig. 4 except for the differences between outer and inner water levels.

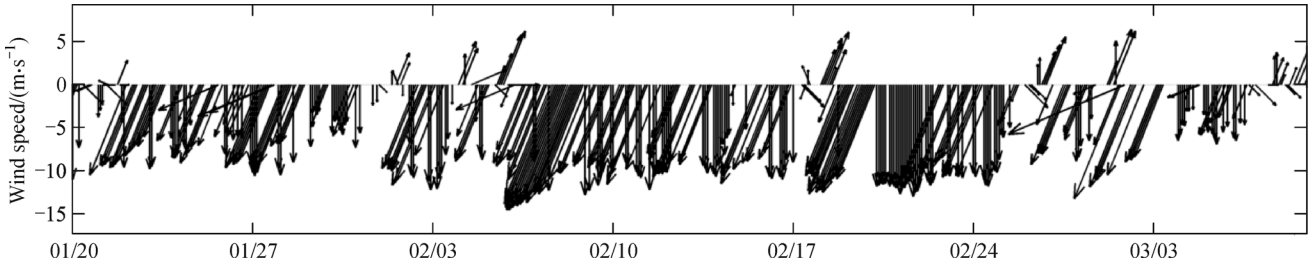

Fig. 6 Wind vector time series observed at the Mazu Buoy. The vectors were plotted every 2 hr.

at a potential connection between them. We first examined the correlation between the two. The wind stress was expected to be a more dynamically relevant variable to influence water-level variability, thus the wind speed was converted to wind stress (Large and Pond, 1981) prior to correlation analysis. A comparison between wind stress and residual water-level time series at individual stations is shown in Fig. 8. It is clearly evident that the wind-stress time series matched fairly well with the residual water-level time series. The correlation coefficient between each pair of the time series exceeded 0.78 at all stations after a 5 hr running average was applied to both time series. This high correlation prompted us to further investigate the interactions between the residual water levels and the contemporaneous winds.

The frequency-dependent coherence between residual water levels and the winds with different directions was analyzed. The wind-stress time series was temporally interpolated to be aligned with water-level observations. We defined the wind direction to have an inclination angle of 0° for an eastward wind (i.e., westerly), and the angle increased counterclockwise (see the schematic arrows in Fig. 1). This definition was intended to facilitate studying the coherence between residual water levels and winds

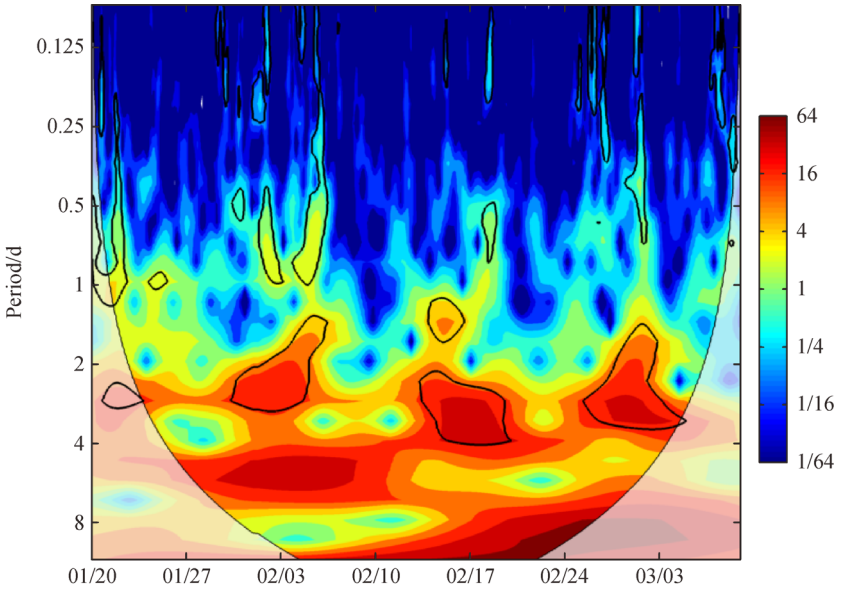

Fig. 7 Wavelet power spectrum of the wind speed observed at the Mazu Buoy. The thick black contours enclose regions within which the wavelet power was significant at the 95% confidence level assuming a red-noise null hypothesis. Regions where the edge effects became important are shaded with a light color.

blowing from all directions. It is shown in Fig. 9 that the residual water level at individual stations was highly coherent with the wind stress at a broad frequency band ranging from approximately 0.1 to 0.8 cpd. The inclination angles corresponding to high coherence ranged from 10 to 40° (or plus 180°), which meant that the winds were blowing in the southwest-northeast direction, roughly parallel to the orientation of the coastline near Sansha Bay (Fig. 1). In other words, the residual water level at individual stations was primarily affected by the alongshore wind at synoptic time scales.

The coherence between the wind stress and residual water-level differences between the outer and inner bay is shown in Fig. 10. In contrast to the results in Fig. 9, Fig. 10 reveals several narrow frequency bands with high coherence. There was evidence that the water-level difference was highly coherent with the wind stress at a frequency of approximately 0.5 cpd, but the high coherence did not correspond to a unique wind direction. A weaker but discernible high-coherence band was also found near the diurnal frequency. The inclination angles corresponding to high coherence ranged from 80 to 120° (or plus 180°), roughly perpendicular to the coastline nearby, hinting that the sea breeze might be playing a role in modulating the residual water-level difference between the outer and inner bay.

5.3 Wavelet analysis of residual water levels and the wind

The cross-wavelet transform and wavelet-coherence analysis of residual water levels and the wind stress are now used to gain further insights into their interactions. The former is intended to find regions of high common power of the time series in the time-frequency space, while the latter is intended to find regions where the two time series co-vary, albeit with low common power (Grinsted et al., 2004).

Based on the results shown in Figs. 9 and 10, we examined the interactions between residual water levels and the alongshore wind (with an inclination angle of 20°), and the interactions between residual water-level difference and the cross-shore wind (with an inclination angle of 100°). The observed wind stresses were projected to obtain the alongshore and cross-shore components. Given that the wind data were collected every 1 hr, both the wind-stress and water-level time series were low-pass filtered to suppress high-frequency signals with periods shorter than 2 hr prior to wavelet analysis.

The cross-wavelet and wavelet-coherence spectra of the alongshore wind and residual water levels for individual stations are shown in Fig. 11. Overall, the spectral patterns were qualitatively similar amongst stations. The cross-wavelet spectra indicated relatively high power at a narrow frequency band corresponding to a period of 0.5 d and at a broad frequency band with periods longer than 1 d (left panels of Fig. 11). This high-common-power broad band was also seen in the coherence analysis as shown in Fig. 9, and was attributed to synoptic weather changes. The pattern of wavelet-coherence spectra closely resembled that of the cross-wavelet spectra, in particular at the synoptic broad frequency band, although more intermittency was found at the high-coherence band with a period of 0.5 d (right panels of Fig. 11). The phase spectra from the cross-wavelet and wavelet-coherence analyses both

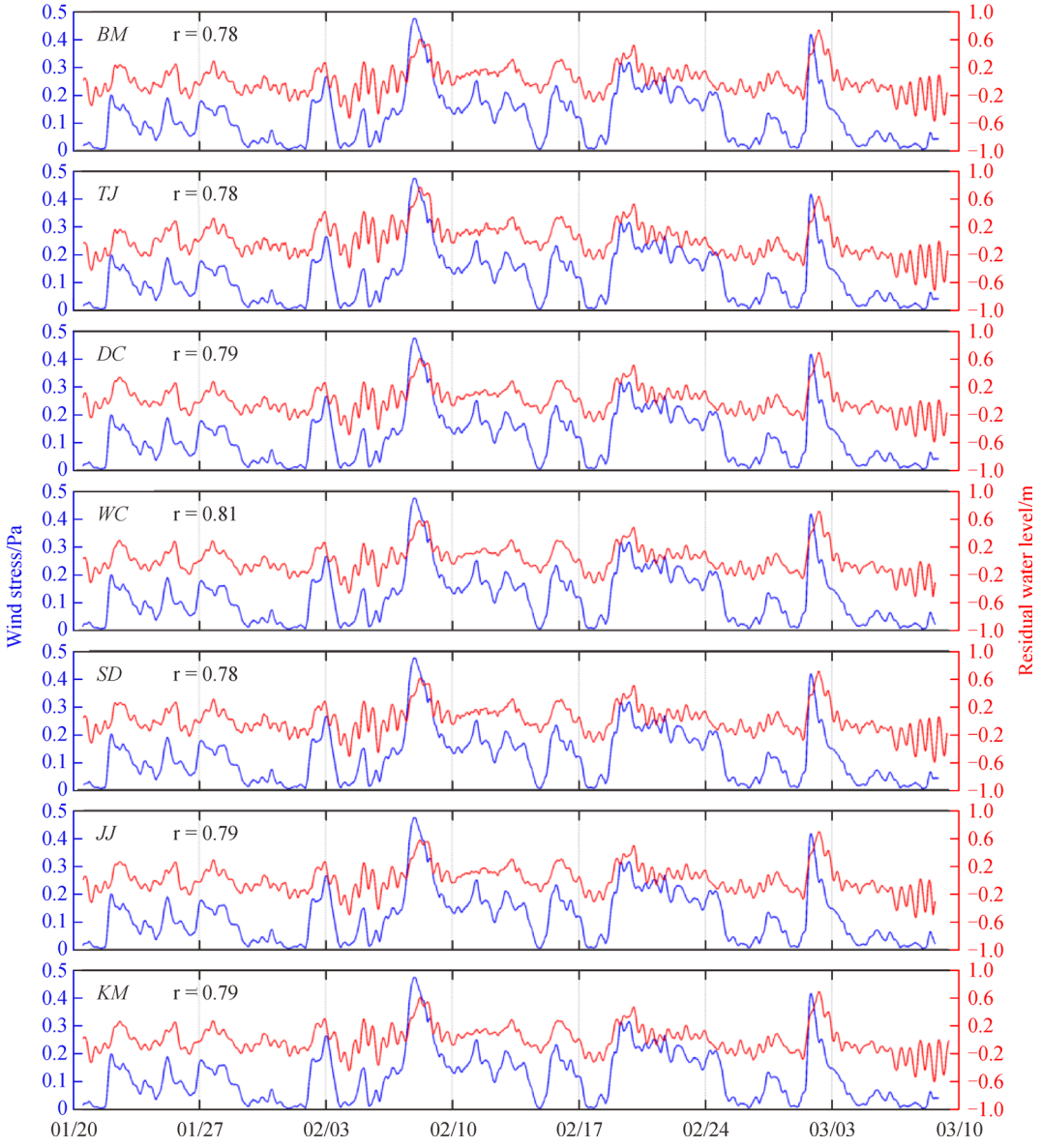

Fig. 8 Time series of wind stress (blue; in Pa) and residual water levels (red; in m) at individual stations. A 5 hr running average was applied to both time series. The correlation coefficient for each pair of the smoothed time series is shown on the upper-left corner of each panel.

suggested that the alongshore wind and individual residual water levels were approximately out of phase (see arrows in Fig. 11). This could be interpreted by the classic Ekman transport theory, i.e., a southwesterly (northeasterly) wind was associated with offshore (onshore) volume transport and hence lower (higher) residual water level within the bay.

The cross-wavelet and wavelet-coherence spectra of the cross-shore wind and residual water-level difference between the outer and inner bay are shown in Fig. 12. The cross-wavelet spectra (left panels of Fig. 12) were similar to those shown in the left panels of Fig. 11, i.e., high common power at periods of 0.5 d and longer than 1 d. By contrast, the wavelet-coherence spectra showed rather different patterns. Most notably, the high-coherence broad band with periods longer than 1 d did not appear, and were replaced by several narrow frequency bands with high coherence (right panels of Fig. 12). This is consistent with the results shown in Fig. 10. These narrow bands showed intermittent high coherence occurring at periods of approximately 0.5 d, 1 d, and 2−6 d. The phase spectra did not show a persistent lead-lag relationship between water levels and the wind at frequencies higher than the diurnal frequency (see arrows in Fig. 12); at lower frequency bands, the cross-shore wind led the water-level difference by a certain period. This meant that the onset of shore-normal winds would subsequently set up a pressure gradient along the downwind direction. Specifically, the

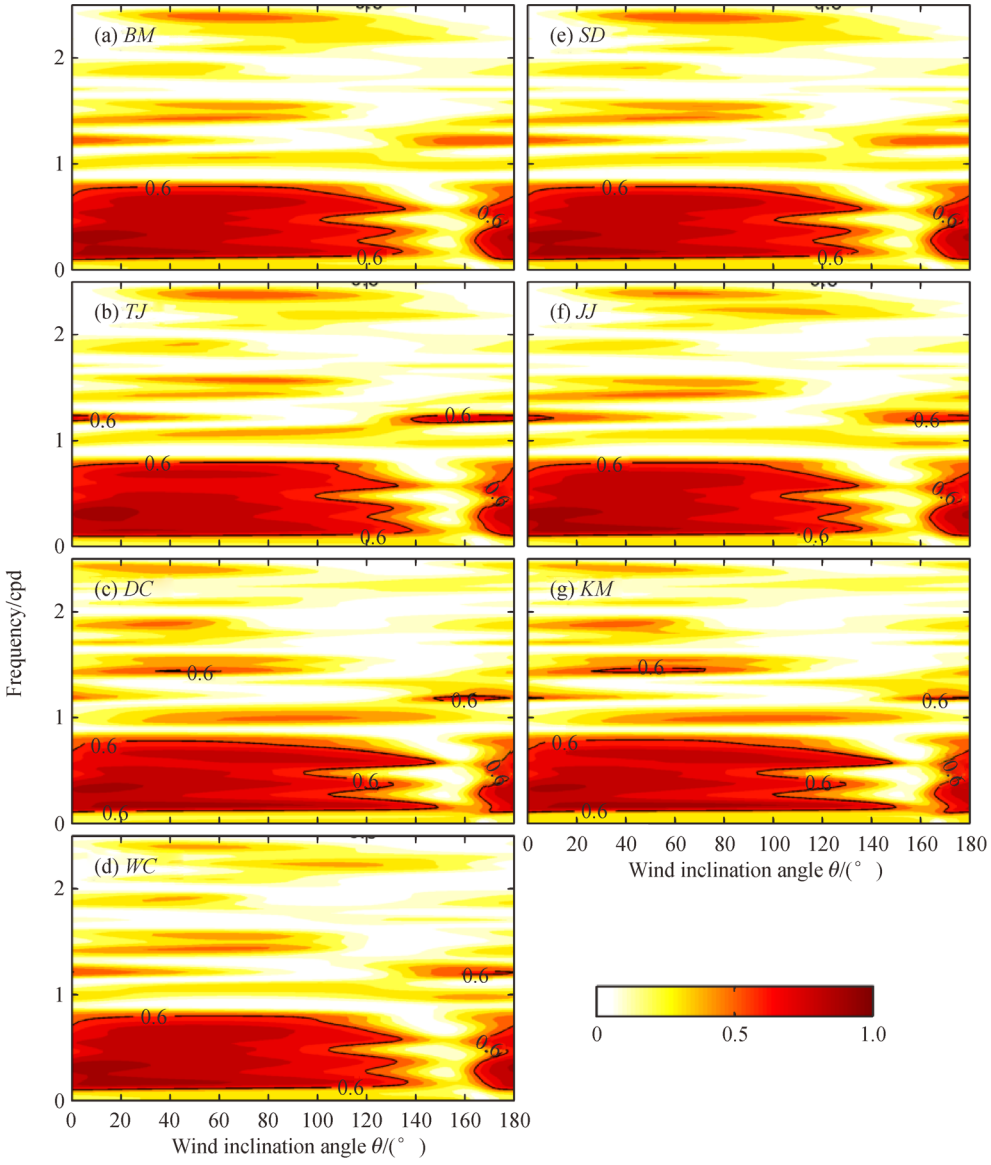

Fig. 9 Coherence between residual water level at individual stations and the wind stress with different directions. The abscissa denotes the wind direction; and increasing angles correspond to wind directions and rotate counterclockwise, with zero-degree denoting the westerly wind.

onshore (offshore) wind was associated with a smaller (larger) residual water-level difference between the outer and inner bay.

Based on the wavelet-coherence analysis, the land-sea breeze seemed to play a limited role in modulating residual water-level difference. This might be attributed to two reasons: (i) The modulation in sea level caused by the dominating monsoon was overwhelming, and the monsoon was roughly alongshore. This made the effect caused by the cross-shore wind on water-level variation inconspicuous. (ii) The difference in land-sea surface temperature was relatively small in winter, which was unfavorable for the formation of land-sea breeze. It was interesting to note that at the diurnal frequency, the cross-shore wind and residual water-level difference were more coherent (see right panels of Fig. 12) for the periods 29 January to 4 February, 2013 (Days 28 to 34 after 1 January, 2013), 14 to 17 February (Days 44 to 47), and 26 February to 5 March (Days 56 to 63). Such short periods happened to coincide with the monsoon relaxation periods (Fig. 6), and this might have been beneficial to the formation of a land-sea breeze.

6 Summary and discussion

Using the wind data observed at the Mazu Buoy and the water level time series collected at seven stations along the

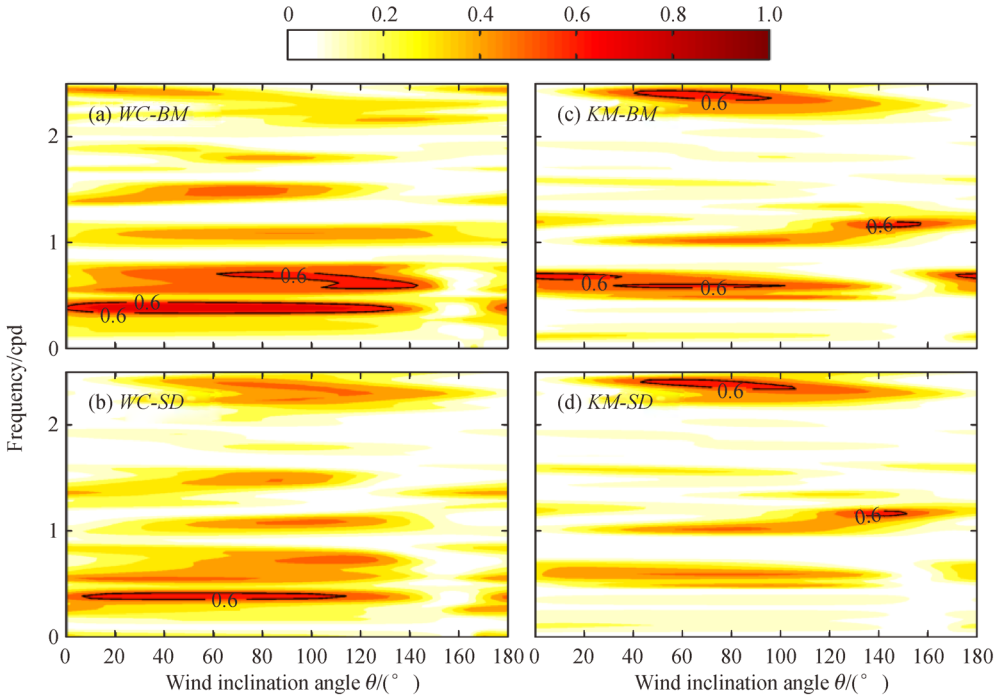

Fig. 10 Similar to Fig. 9 but for residual water-level difference between the outer and inner bay.

coasts of Sansha Bay and its adjacent waters, we analyzed the characteristics of water-level variability caused by tides and winds. The interactions between the large-scale wind forcing and residual water levels were of our particular interest. The main findings are summarized as follows:

(i) At super- to near-inertial frequencies, tides dominated the water-level variations in our study region. The range of raw water levels was larger than that of residual water levels by a factor of 6 to 7. The raw water-level time series were mainly characterized by semi-diurnal tides, followed by diurnal tides. The residual water-level time series at all stations shared a rather similar shape in terms of time variation. The raw water-level difference between the outer and inner bay had similar frequencies as the individual raw water level, but the tidal range was much smaller. The residual water-level difference indicated more high-frequency variability, and the elevation range was generally less than 0.4 m.

(ii) Residual water-level time series at individual stations was well correlated with the observed wind-stress time series. The correlation coefficient was greater than 0.78 at all stations after a moderate smoothing. This meant that the large-scale wind forcing, as well as tides, was another factor which modulated the variability of water levels in the study region. The spectral analysis indicated that both the wind speed and residual water levels had periods of 0.5 d and 2−3 d. They were also highly coherent at a broad frequency band potentially associated with synoptic weather changes (with periods of 1−8 d). The coherence analysis suggested that that residual water level at individual stations was primarily controlled by alongshore winds, while the cross-shore winds acted more on the residual water-level difference.

(iii) The cross-wavelet and wavelet-coherence analyses indicated that the residual water level at individual stations was more coherent, and out-of-phase, with alongshore winds. The high coherence was persistent at a synoptic time scale whereas it was more intermittent at periods of 0.5−1 d. The out-of-phase feature could be explained with the Ekman convergence/divergence. By contrast, the residual water-level difference between the outer and inner bay was more coherent with the cross-shore winds at narrow, discrete frequency bands. The lead-lag relationship was not clear at the super-inertial time scale, but the cross-shore winds led the residual water-level difference by a certain period at the sub-inertial time scale. The cross-shore land-sea breeze seemed to play a limited role in modulating the residual water-level difference probably due to the overwhelming alongshore monsoon. It was interesting to see that the cross-shore winds were more coherent with the residual water-level difference at the diurnal period when the monsoon is experiencing its relaxation period, implying that the role of the land-sea breeze might need to be taken into consideration during such relaxation periods. In fact, the residual water-level difference between the outer and inner bay showed the footprint of the spatial difference in the mean sea levels. Thus, it was probably more meaningful to be examined over a long-term period (say longer than several years) and to find the drivers acting over the same period (Lin et al.,

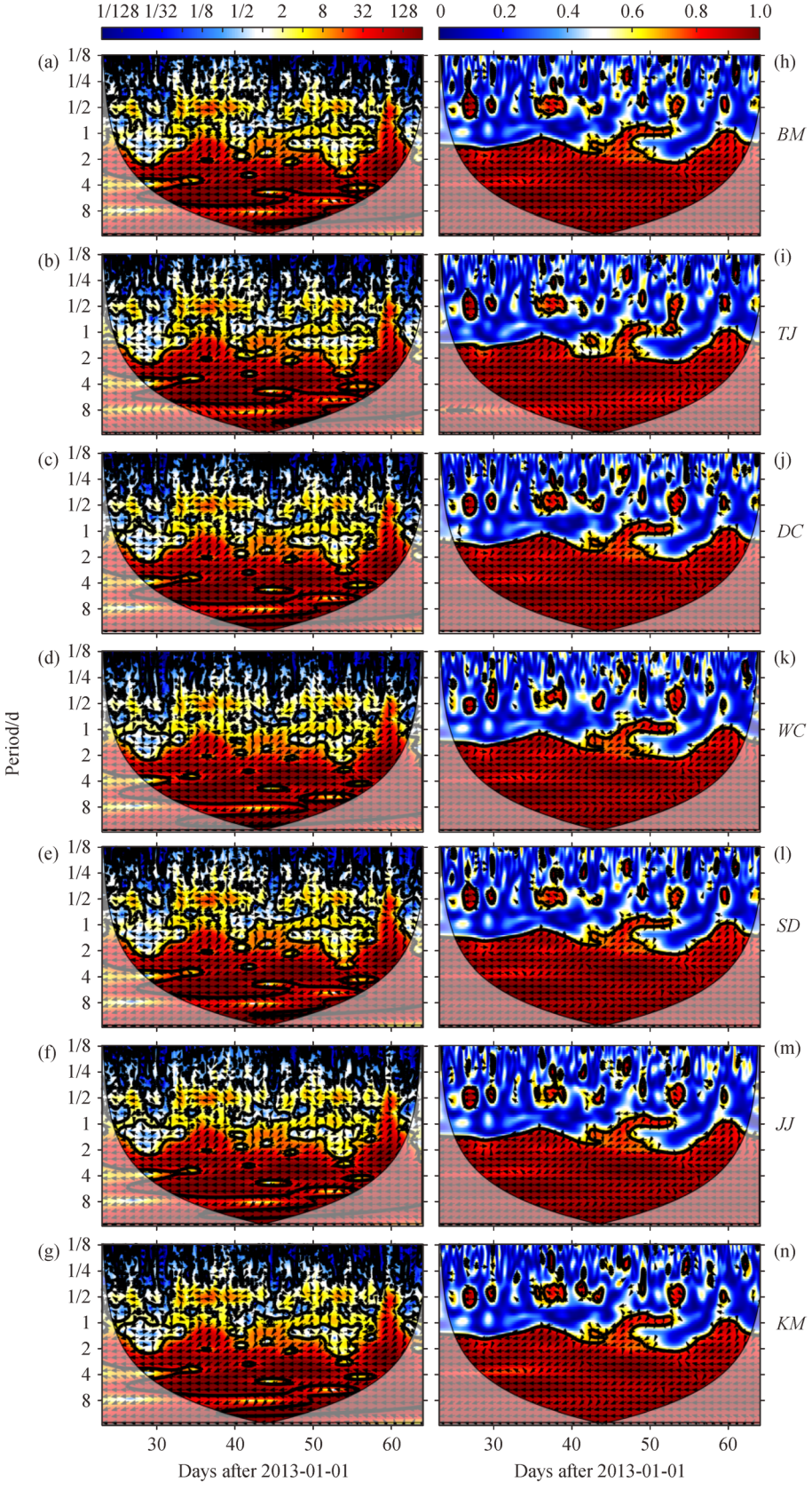

Fig. 11 Cross-wavelet (left) and wavelet-coherence (right) spectra of the alongshore wind and residual water levels for individual stations. The thick black contours enclose regions within which the wavelet power was significant at the 95% confidence level assuming a red-noise null hypothesis. Regions where the edge effects became important are shaded with white. Black arrows denote the phase lag between residual water level and the wind: → (←) means in phase (out of phase); ↓ (↑) means water level leads (lags) the wind changes by 90°.

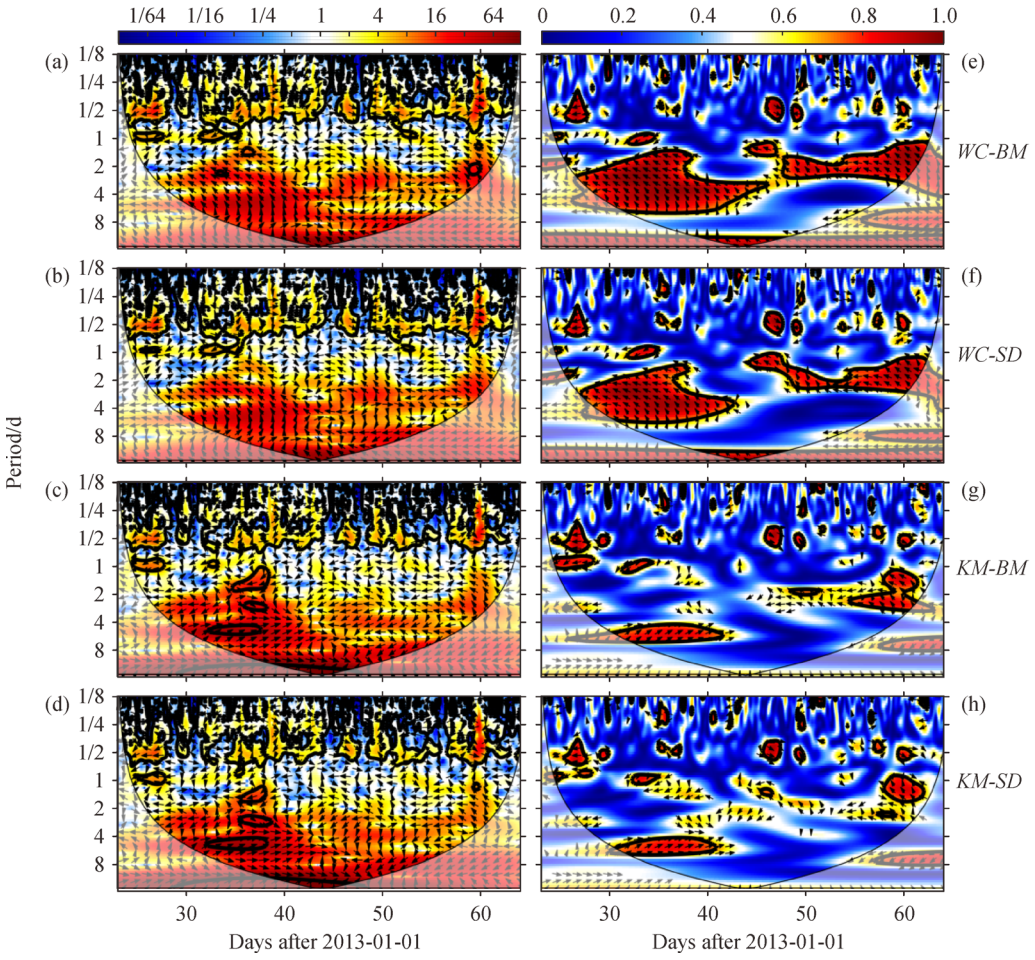

Fig. 12 Cross-wavelet (left) and wavelet-coherence (right) spectra of the cross-shore wind and residual water-level difference between the outer and inner bay. The formats are similar to Fig. 11.

2015). Nevertheless, it was not possible to do that in this study given the water-level time series covering a period of less than two months.

The wind vectors used in the present study were measured at a reference location, Mazu Buoy, and are assumed to be spatially uniform over stations where the water-level time series were collected. However, frontal-scale wind fields are demonstrated to be important when considering ocean responses (Chuang and Wiseman, 1983). The next step, therefore, would be to have a better representation of the wind field in the study region, and to provide a more accurate description of the ocean responses to the wind forcing.

Acknowledgements This work is supported by the Public Science and Technology Research Funds Projects of Ocean under contract No. 201205009-2, the National Natural Science Foundation of China (Grant Nos. 41276006 and U1405233), and the Open Fund of the Key Laboratory of Ocean Circulation and Waves, Chinese Academy of Sciences under contract No. KLOCAW1408. We thank Professor John Hodgkiss of The University of Hong Kong for assistance with English.

References

Cai Q, Du Q, Qian X, Xu C (2007). Comprehensive evaluation on marine ecological environment of Sansha Bay in Fujian, China. Acta Oceanol Sin, 29(2): 156–160 (in Chinese)

Chuang W S, Wiseman W J Jr (1983). Coastal sea level response to frontal passages on the Louisiana-Texas shelf. J Geophys Res, 88 (C4): 2615–2620

Clancy R, Thompson J, Hurlburt H, Lee J (1979). A model of mesoscale air-sea interaction in a sea breeze-coastal upwelling regime. Mon Weather Rev, 107(11): 1476–1505

Craig P D (1989a). Constant-eddy-viscosity models of vertical structure forced by periodic winds. Cont Shelf Res, 9(4): 343–358

Craig P D (1989b). A model of diurnally forced vertical current structure near 30 latitude. Cont Shelf Res, 9(11): 965–980

Csanady G T (1980). Longshore pressure gradients caused by offshore wind. J Geophys Res, 85(C2): 1076–1084

Csanady G T (1982). Circulation in the Coastal Ocean. Springer: Dordrecht, 279

Farge M (1992). Wavelet transforms and their applications to turbulence.

Annu Rev Fluid Mech, 24(1): 395–458

Gallop S L, Verspecht F, Pattiaratchi C B (2012). Sea breezes drive currents on the inner continental shelf off southwest Western Australia. Ocean Dyn, 62(4): 569–583

Grinsted A, Moore J C, Jevrejeva S (2004). Application of the cross wavelet transform and wavelet coherence to geophysical time series. Nonlinear Process Geophys, 11(5/6): 561–566

Hasselmann K (1976). Stochastic climate models- Part I: Theory. Tellus, Ser A, Dyn Meterol Oceanogr, 28(6): 473–485

Large W, Pond S (1981). Open ocean momentum flux measurements in moderate to strong winds. J Phys Oceanogr, 11(3): 324–336

Lau K, Weng H (1995). Climate signal detection using wavelet transform: how to make a time series sing. Bull Am Meteorol Soc, 76(12): 2391–2402

Lin H, Thompson K R, Huang J, Véronneau M (2015). Tilt of mean sea level along the Pacific coasts of North America and Japan. J Geophys Res, 120(10): 6815–6828

Lin J, Chen R, Lin M, Dai Y (1998). Distribution of zooplankton in Sansha Bay and its comparison with that in Xinghua Bay and Dongshan Bay. J Oceanogr Taiwan, 17(4): 426–432 (in Chinese)

Liu P C (1994). Wavelet spectrum analysis and ocean wind waves. In: Foufoula-Georgiou E, Kumar P, eds. Wavelets in Geophysics. Academic Press: New York, 151–166

Mann M E, Lees J M (1996). Robust estimation of background noise and signal detection in climatic time series. Clim Change, 33(3): 409–445

Meyers S D, Kelly B G, O'Brien J J (1993). An introduction to wavelet analysis in oceanography and meteorology: with application to the dispersion of Yanai waves. Mon Weather Rev, 121(10): 2858–2866

Morlet J (1983), Sampling theory and wave propagation. In: Chen C H, ed. Issues in Acoustic Signal—Image Processing and Recognition. Springer: Berlin, 233–261

Nam S, Send U (2013). Resonant diurnal oscillations and mean alongshore flows driven by sea/land breeze forcing in the coastal Southern California Bight. J Phys Oceanogr, 43(3): 616–630

Pawlowicz R, Beardsley B, Lentz S (2002). Classical tidal harmonic analysis including error estimates in MATLAB using T_TIDE. Comput Geosci, 28(8): 929–937

Percival D, Walden A (1993). Spectral Analysis for Physical Applications: Multitaper and Conventional Univariate Techniques. Cambridge University Press, 580

Ryan H, Noble M (2007). Sea level fluctuations in central California at subtidal to decadal and longer time scales with implications for San Francisco Bay, California. Estuar Coast Shelf Sci, 73(3−4): 538–550

Simpson J, Hyder P, Rippeth T, Lucas I (2002). Forced oscillations near the critical latitude for diurnal-inertial resonance. J Phys Oceanogr, 32(1): 177–187

Smith R L (1974). A description of current, wind, and sea level variations during coastal upwelling off the Oregon coast, July–August 1972. J Geophys Res, 79(3): 435–443

Thomson D J (1982). Spectrum estimation and harmonic analysis. Proc IEEE, 70(9): 1055–1096

Torrence C, Compo G P (1998). A practical guide to wavelet analysis. Bull Am Meteorol Soc, 79(1): 61–78

Torrence C, Webster P J (1999). Interdecadal changes in the ENSO-monsoon system. J Clim, 12(8): 2679–2690

Vesecky J F, Teague C C, Onstott R G, Daida J M, Hansen P, Fernandez D, Schnepf N, Fischer K (1997). Surface current response to land-sea breeze circulation in Monterey Bay, California as observed by a new multifrequency HF radar. OCEANS'97. MTS/IEEE Conference Proceedings, 2: 1019–1024

Walters R A, Cheng R T, Conomos T J (1985). Time scales of circulation and mixing processes of San Francisco Bay waters. In: Cloern J E, Nichols F H, eds. Temporal Dynamics of an Estuary: San Francisco Bay. Springer: Dordrecht, 13–36

Wang Y, Song Z, Jiang C, Kong J, Liu Q (2009). Numerical and Environmental Studies of Bays in Fujian Province: the Sansha Bay. Beijing: Ocean Press, 283 (in Chinese)

Zhang X, DiMarco S F, Smith D C IV, Howard M K, Jochens A E, Hetland R D (2009). Near-resonant ocean response to sea breeze on a stratified continental shelf. J Phys Oceanogr, 39(9): 2137–2155